



AFRL-RX-WP-JA-2015-0210

**THE POTENTIAL LINK BETWEEN HIGH ANGLE
GRAIN BOUNDARY MORPHOLOGY AND GRAIN
BOUNDARY DEFORMATION IN A NICKEL-BASED
SUPERALLOY (POSTPRINT)**

Jennifer L. W. Carter and Michael J. Mills

Department of Materials Science and Engineering, The Ohio State University

John M. Sosa and Hamish L. Fraser

Center for Accelerated Maturation of Materials, The Ohio State University

Paul A. Shade and Michael D. Uchic

Air Force Research Laboratory, Materials and Manufacturing Directorate

JUNE 2015

Interim Report

Distribution Statement A. Approved for public release: distribution unlimited.

See additional restrictions described on inside pages

STINFO COPY

© 2015 Elsevier B. V.

**AIR FORCE RESEARCH LABORATORY
MATERIALS AND MANUFACTURING DIRECTORATE
WRIGHT-PATTERSON AIR FORCE BASE OH 45433-7750
AIR FORCE MATERIEL COMMAND
UNITED STATES AIR FORCE**

NOTICE AND SIGNATURE PAGE

Using Government drawings, specifications, or other data included in this document for any purpose other than Government procurement does not in any way obligate the U.S. Government. The fact that the Government formulated or supplied the drawings, specifications, or other data does not license the holder or any other person or corporation; or convey any rights or permission to manufacture, use, or sell any patented invention that may relate to them.

Qualified requestors may obtain copies of this report from the Defense Technical Information Center (DTIC) (<http://www.dtic.mil>).

AFRL-RX-WP-JA-2015-0210 HAS BEEN REVIEWED AND IS APPROVED FOR PUBLICATION IN ACCORDANCE WITH ASSIGNED DISTRIBUTION STATEMENT.

//Signature//

MICHAEL D. UCHIC, Project Engineer
Metals Branch
Structural Materials Division

//Signature//

DANIEL J. EVANS, Chief
Metals Branch
Structural Materials Division

//Signature//

ROBERT T. MARSHALL, Deputy Chief
Structural Materials Division
Materials And Manufacturing Directorate

This report is published in the interest of scientific and technical information exchange and its publication does not constitute the Government's approval or disapproval of its ideas or findings.

REPORT DOCUMENTATION PAGE

Form Approved
OMB No. 0704-0188

The public reporting burden for this collection of information is estimated to average 1 hour per response, including the time for reviewing instructions, searching existing data sources, gathering and maintaining the data needed, and completing and reviewing the collection of information. Send comments regarding this burden estimate or any other aspect of this collection of information, including suggestions for reducing this burden, to Department of Defense, Washington Headquarters Services, Directorate for Information Operations and Reports (0704-0188), 1215 Jefferson Davis Highway, Suite 1204, Arlington, VA 22202-4302. Respondents should be aware that notwithstanding any other provision of law, no person shall be subject to any penalty for failing to comply with a collection of information if it does not display a currently valid OMB control number. **PLEASE DO NOT RETURN YOUR FORM TO THE ABOVE ADDRESS.**

| | | | | | | |
|---|--|---|---|--------------------------------------|--|--|
| 1. REPORT DATE (DD-MM-YY) June 2015 | | | 2. REPORT TYPE Interim | | 3. DATES COVERED (From - To) 23 July 2013 – 12 May 2015 | |
| 4. TITLE AND SUBTITLE THE POTENTIAL LINK BETWEEN HIGH ANGLE GRAIN BOUNDARY MORPHOLOGY AND GRAIN BOUNDARY DEFORMATION IN A NICKEL-BASED SUPERALLOY (POSTPRINT) | | | | | 5a. CONTRACT NUMBER FA8650-10-D-5226-0003 | |
| | | | | | 5b. GRANT NUMBER | |
| | | | | | 5c. PROGRAM ELEMENT NUMBER 62102F | |
| 6. AUTHOR(S) See back. | | | | | 5d. PROJECT NUMBER 4347 | |
| | | | | | 5e. TASK NUMBER | |
| | | | | | 5f. WORK UNIT NUMBER X0LX | |
| 7. PERFORMING ORGANIZATION NAME(S) AND ADDRESS(ES) See back. | | | | | 8. PERFORMING ORGANIZATION REPORT NUMBER | |
| 9. SPONSORING/MONITORING AGENCY NAME(S) AND ADDRESS(ES) Air Force Research Laboratory Materials and Manufacturing Directorate Wright-Patterson Air Force Base, OH 45433-7750 Air Force Materiel Command United States Air Force | | | | | 10. SPONSORING/MONITORING AGENCY ACRONYM(S) AFRL/RXCM | |
| | | | | | 11. SPONSORING/MONITORING AGENCY REPORT NUMBER(S) AFRL-RX-WP-JA-2015-0210 | |
| 12. DISTRIBUTION/AVAILABILITY STATEMENT Distribution Statement A. Approved for public release: distribution unlimited. | | | | | | |
| 13. SUPPLEMENTARY NOTES Journal article published in <i>Materials Science & Engineering A</i> 640 (2015) 280-286. © 2015 Elsevier B. V. The U.S. Government is joint author of the work and has the right to use, modify, reproduce, release, perform, display or disclose the work. This report contains color. The final publication is available at http://dx.doi.org/10.1016/j.msea.2015.05.031 . | | | | | | |
| 14. ABSTRACT Focused ion beam (FIB) based serial sectioning was utilized to characterize the morphology of two high angle grain boundaries (HAGB) in a nickel based superalloy, one that experienced grain boundary sliding (GBS) and the other experienced strain accumulation, during elevated temperature constant stress loading conditions. A custom script was utilized to serial section and collection-induced secondary electron images from the FIB-SEM system. The MATLAB based MIPAR™ software was utilized to align, segment and reconstruct 3D volumes from the sectioned images. Analysis of the 3D data indicates that the HAGB that exhibited GBS had microscale curvature that was planar in nature, and local serrations on the order of $\pm 150\text{nm}$. In contrast, the HAGB that exhibited strain accumulation was not planar and had local serrations an order of magnitude greater than the other grain boundary. It is hypothesized that the serrations and the local grain boundary network are key factors in determining which grain boundaries experience GBS during creep deformation. | | | | | | |
| 15. SUBJECT TERMS serial sectioning, 3D reconstruction, nickel-based superalloys, grain boundary sliding | | | | | | |
| 16. SECURITY CLASSIFICATION OF: | | | 17. LIMITATION OF ABSTRACT: SAR | 18. NUMBER OF PAGES 11 | 19a. NAME OF RESPONSIBLE PERSON (Monitor) Michael D. Uchic 19b. TELEPHONE NUMBER (Include Area Code) (937) 255-0594 | |
| a. REPORT Unclassified | b. ABSTRACT Unclassified | c. THIS PAGE Unclassified | | | | |

REPORT DOCUMENTATION PAGE Cont'd

6. AUTHOR(S)

Jennifer L. W. Carter and Michael J. Mills - Department of Materials Science and Engineering, The Ohio State University

John M. Sosa and Hamish L. Fraser - Center for Accelerated Maturation of Materials, The Ohio State University

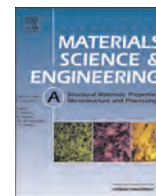
Paul A. Shade and Michael D. Uchic - Air Force Research Laboratory, Materials and Manufacturing Directorate

7. PERFORMING ORGANIZATION NAME(S) AND ADDRESS(ES)

Department of Materials Science and Engineering
The Ohio State University
Columbus, OH 44321

Center for Accelerated Maturation of Materials
The Ohio State University
Columbus, OH 44321

Air Force Research Laboratory
Materials and Manufacturing Directorate
AFRL/RXCM
Wright-Patterson AFB, OH 45433



The potential link between high angle grain boundary morphology and grain boundary deformation in a nickel-based superalloy

Jennifer L.W. Carter^{a,*}, John M. Sosa^b, Paul A. Shade^c, Hamish L. Fraser^b,
Michael D. Uchic^c, Michael J. Mills^a

^a Department of Materials Science and Engineering, The Ohio State University, Columbus, OH 44321, USA

^b Center for Accelerated Maturation of Materials, The Ohio State University, Columbus, OH 44321, USA

^c Air Force Research Laboratory, Materials & Manufacturing Directorate, AFRL/RXCM, Wright-Patterson AFB, Dayton, OH 45433, USA

ARTICLE INFO

Article history:

Received 2 April 2015

Accepted 12 May 2015

Available online 18 May 2015

Keywords:

Serial sectioning

3D reconstruction

Nickel-based superalloys

Grain boundary sliding

ABSTRACT

Focused ion beam (FIB) based serial sectioning was utilized to characterize the morphology of two high angle grain boundaries (HAGB) in a nickel based superalloy, one that experienced grain boundary sliding (GBS) and the other experienced strain accumulation, during elevated temperature constant stress loading conditions. A custom script was utilized to serial section and collect ion induced secondary electron images from the FIB SEM system. The MATLAB based MIPARTM software was utilized to align, segment and reconstruct 3D volumes from the sectioned images. Analysis of the 3D data indicates that the HAGB that exhibited GBS had microscale curvature that was planar in nature, and local serrations on the order of ± 150 nm. In contrast, the HAGB that exhibited strain accumulation was not planar and had local serrations an order of magnitude greater than the other grain boundary. It is hypothesized that the serrations and the local grain boundary network are key factors in determining which grain boundaries experience GBS during creep deformation.

© 2015 Elsevier B.V. All rights reserved.

1. Introduction

The creep deformation in polycrystalline nickel based superalloys is a heterogeneous process, the primary mechanism that controls this deformation is the interaction of dislocations with the γ' precipitate distribution, while ultimate creep life is dependent on damage accumulation near grain boundaries [1]. Predicting the behavior of polycrystalline materials by simulation techniques [2,3] is dependent on producing relevant experimental data at appropriate time and length scales to validate the predicted behavior. Recent experiments on nickel based superalloys that quantify local deformation at grain boundaries in two dimensions (2D) [4] and three dimensions (3D) [5] have confirmed that experiments that capture only the 2D deformation fields can provide statistical insight but are insufficient to fully validate 3D deformation models. The deformation behavior of grain boundaries is a function of the grain boundary misorientation, the orientation of the grain boundary with respect to the loading direction, the morphology of

the grain boundary, and the local stress state which can be very different from the far field boundary conditions [5]. These last three parameters are difficult to characterize with scanning electron microscopy (SEM) or transmission electron microscopy (TEM) because these techniques only provide a single projection of the grain boundary structure. Therefore, complete characterization of grain boundaries requires collection of 3D data through a technique such as serial sectioning. Full field strain mapping and grain boundary sliding (GBS) measurements from discrete offsets in grid markers indicate that some grain boundaries in nickel based superalloys experience strain accumulation while other grain boundaries exhibit GBS when the material is subjected to creep conditions [6]. No conclusive evidence could be found that either of these types of behaviors could be predicted based on grain boundary misorientation or the orientation of boundary projections in SEM images with respect to the tensile axis [7]. This led to the hypothesis that grain boundary structure and sub surface grain neighborhood also play a pivotal role in dictating the local deformation response at grain boundaries. In this study, two different high angle grain boundaries (HAGB) were characterized by focused ion beam (FIB) serial sectioning: one exhibited grain boundary sliding, and the other exhibited strain accumulation during creep conditions.

* Corresponding author. Now at the Department of Materials Science and Engineering, Case Western Reserve University, Cleveland, OH 44106, USA.

E-mail address: jennifer.w.carter@case.edu (J.L.W. Carter).

2. Experimental

Creep testing: Constant load, elevated temperature testing was conducted in an SEM under the following conditions: 700 °C and 1100 MPa. Specimens were polished and initial grain boundary locations were quantified prior to testing using electron back scatter diffraction (EBSD). A speckle pattern was subsequently applied to the samples to enable digital image correlation analysis of surface deformation fields. After testing, high resolution images were acquired and analyzed to quantify the contribution of grain boundary sliding (GBS) to plastic strain accommodation. Details of the sample preparation and experimental results are presented elsewhere [6,8]. From the many boundaries identified, two high angle grain boundaries were selected for 3D characterization by serial sectioning. One exhibited strain accumulation with no GBS and the other exhibited GBS but no strain accumulation beyond average macroscopic strain state, as shown in Fig. 1a and b respectively.

Sample preparation: The 3D structure of the grain boundaries shown in Fig. 1 was investigated through serial sectioning using an FEI Nova 600 SEM FIB. Micrometer scale volumes of material were extracted and each placed on an molybdenum OmniProbe grid using an OmniProbe in situ micromanipulation system in a manner similar to thin foil preparation [9], Fig. 2 shows one of the volumes prepared just prior to lift out from the bulk sample. This extraction method was necessary in order to minimize the negative effects due to redeposition during serial sectioning. First a platinum cap was deposited over the area of interest, and then trenches were milled along three faces of the volume. Once trenches were cut, the sample was under cut on two sides to create a cantilever beam of material. The volume was attached to the OmniProbe in situ micromanipulation needle using platinum deposition and then the sample connection to the bulk material was severed. Next, a molybdenum OmniProbe Grid was attached with silver painted to an SEM stub and inserted flat into the SEM FIB chamber such that when imaged with the electron source, the grid looked like what is presented in Fig. 3. A molybdenum grid was used because it mills more slowly than conventional copper grids. The sample was then attached to the end of one of the grid fingers using platinum deposition.

A custom script utilizing FEI Runscript software was used to automate the serial sectioning process, and consisted of cross section milling, collection of ion induced secondary electron (ISE)

images, and repositioning of the stage between the two conditions [10]. The FIB column was set to an accelerating voltage of 30 kV, and the current was switched between 2.8 nA for cross section milling and 0.47 nA for ISE imaging. The sample stub was mounted on a 45° pre tilted specimen holder in order to enable the script to perform both cross section milling and normal incidence imaging of the cross section surface, which required both rotation and tilting of the microscope stage, as illustrated in Fig. 3. A pair of circular fiducial marks were used for automated alignment purposes. ISE images were used for this study because ISE images displayed significant channeling contrast that accentuated the crystallographic orientations of the grain structures, making it possible to construct automated segmentation processes that define the grain boundary morphology.

Two grain boundary volumes were extracted for serial section characterization, in both cases, the section thickness was approximately 50 nm. The sample containing the HAGB that exhibited GBS was reconstructed from 116 slices with each image having in plane resolution of 223 pixels/μm, resulting in a 406 μm³ volume. This leads to highly anisotropic voxels 4.48 × 4.48 × 50 nm in size. The sample containing the HAGB that exhibited strain accumulation was approximately 2080 μm³ in size and was reconstructed from 110 slices with each image having in plane resolution of 24 pixels/μm. This leads to slightly anisotropic voxels 41.6 × 41.6 × 50 nm in size. This larger volume contained several grain boundaries of interest for reconstruction. In this case, normal incidence images did not provide adequate channeling

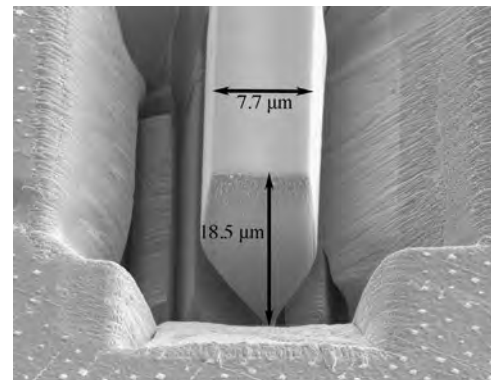


Fig. 2. Secondary electron micrograph showing the platinum capped serial sectioning sample ready for lift-off from the bulk material.

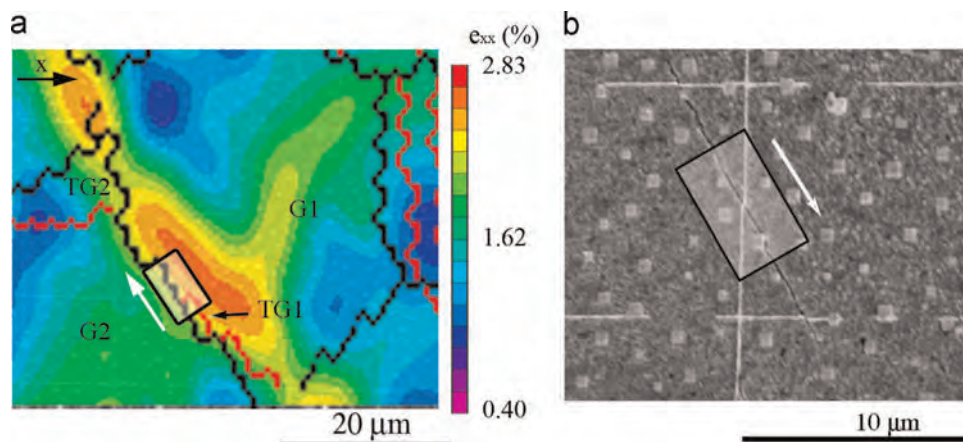


Fig. 1. (a) A DIC strain map with overlaid grain boundaries determined by EBSD prior to deformation (the black lines are HAGB and red lines are annealing twins) shows that the HAGB between grains 1 and grain 2 (G1–G2) experienced strain accumulation, also visible are annealing twins in G1 and G2 (TG1 and TG2 respectively). The (b) secondary electron SEM image highlights the HAGB that experienced GBS as measured via the offset in hafnium oxide grid lines (white) deposited prior to deformation. Rectangular boxes indicate volumes selected for serial sectioning, and white arrows indicate the sectioning direction. (For interpretation of the references to color in this figure caption, the reader is referred to the web version of this paper.)

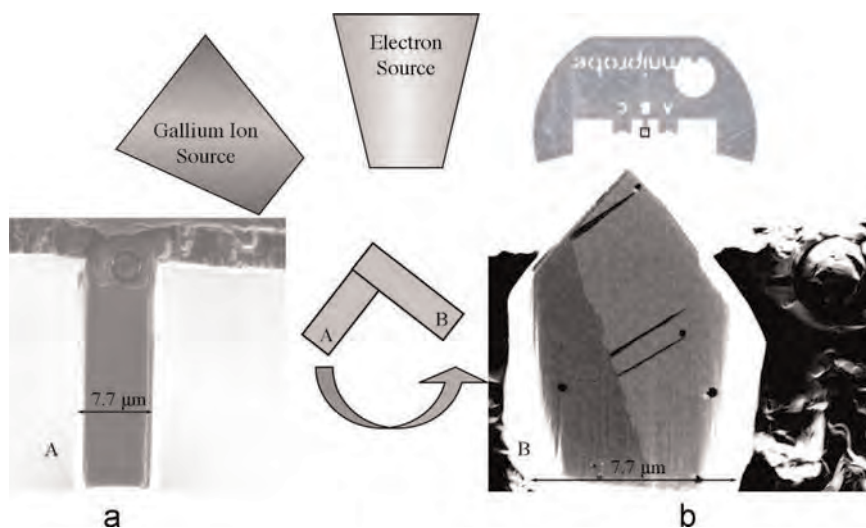


Fig. 3. Schematic showing sample rotation during image collection. (a) First the sample is oriented for sectioning with the ion beam normal to the long axis of the finger (parallel to the milling face), and then (b) the sample is rotated 180° for ion beam imaging of the milled surface. Also shown is the placement of the sample on the OmniProbe grid, as viewed from the electron source.

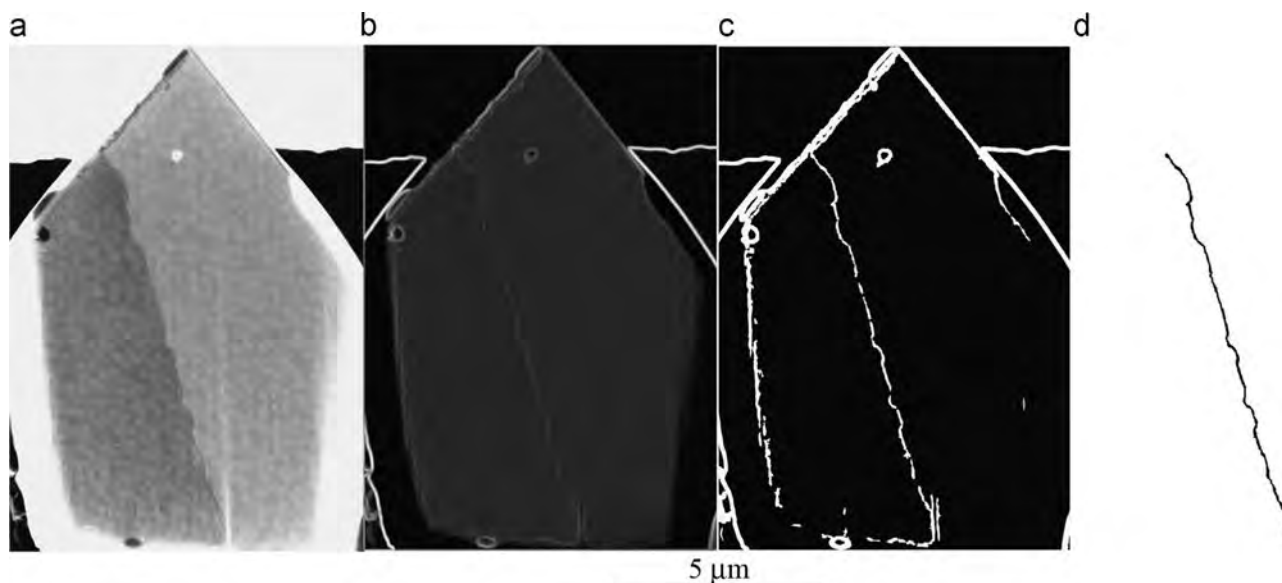


Fig. 4. Segmentation process from the (a) raw image by (b) applying a standard deviation filter of 9×9 pixels, (c) boundary identification with a global threshold and (d) final grain boundary trace after watershed and manual removal of spurious data points.

contrast between adjacent grains; instead images were acquired at an oblique angle of 74° to the surface to maximize the channeling contrast differences between adjacent grains. These images were post processed to remove image foreshortening in the tilt direction using a correction factor of $1/\cos(\theta)$ in the vertical direction, where θ was 16° .

3D volume reconstruction: 3D volumes were reconstructed from the ISE images using the MIPARTM software package [11]. Reconstructions were conducted utilizing the following general steps: image alignment, image segmentation, and boundary identification. Each volume required slightly different processing for automated segmentation and boundary identification. The GBS sliding volume was processed using the following algorithms. First, cross correction was utilized to align the stack of images within a subpixel. Next, a levels adjustment was applied to stretch the intensity histogram to maximize feature enhancement, and a standard deviation filter was applied where every pixel was

re labeled with the standard deviation of its 11×11 pixel neighborhood. This served to highlight pixels near the grain boundary, as the standard deviation of these pixel neighborhoods is considerably higher than pixels in the grain interiors, Fig. 4b. Next, binary image segmentation was performed by applying a user defined global threshold to highlight the grain boundaries, Fig. 4c. In some slices the boundary was artificially discontinuous, and watershed segmentation was employed to fill in most of these discontinuities [12–15]. Pixel clusters not belonging to the boundary were removed by rejecting any objects below a size threshold of 100 pixels. Any remaining pixel clusters were manually removed and remaining discontinuous boundary segments were manually connected, Fig. 4d. This procedure was applied to each slice and resulting binary images were stacked to produce a 3D volume of non cubic voxels.

At this point, the grain boundary network was represented in each 2D image as thin lines (1–2 pixels thick) separating the grain

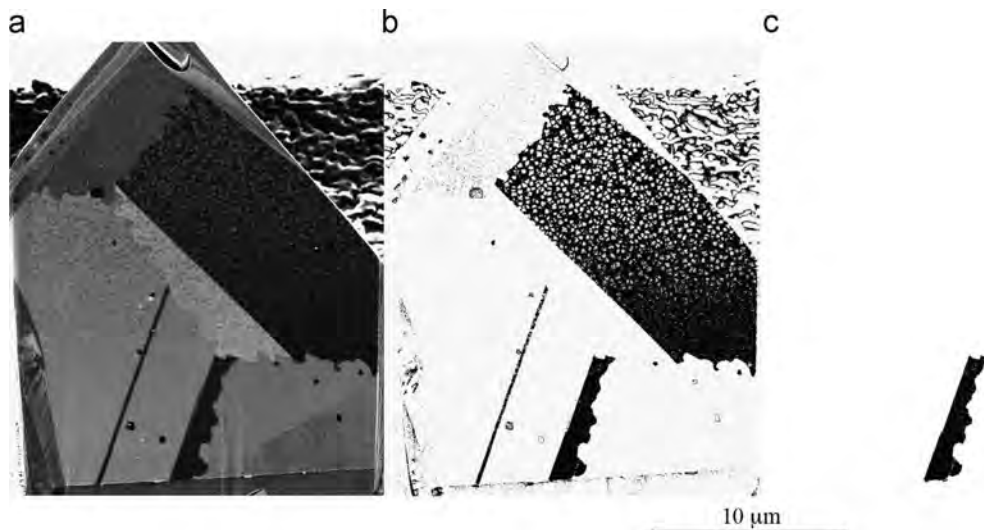


Fig. 5. Segmentation process demonstrated by showing the (a) raw image (b) after applying a global intensity threshold, (c) removing spurious data points with a size threshold and (d) inspected final grain area.

interiors. Although the boundary was fully continuous within each section (i.e. the imaging plane), the boundary was not continuous in 3D due to the anisotropic voxel dimensions and therefore, the grains could not be automatically defined as separate objects using connected component labeling. To create a continuous 3D boundary that fully separated the grains, a 3D watershed algorithm was applied. In contrast with the 2D watershed step, no manual intervention was required after this step. A closed surface was constructed from the voxelized boundaries and this surface was smoothed using a smoothing kernel of $3 \times 3 \times 3$ pixels to facilitate visualization.

In addition to the grain boundary, carbides and deformation twins were also segmented and visualized using algorithms similar to those employed on the grain boundary network. The different segmentations were merged and visualized to create a composite dataset where all microstructural features and their interactions could be analyzed.

The strain accumulation boundary volume proved to be more difficult to process for automated boundary identification. The standard deviation filter was not effective for this data set because of the stronger ISE contrast variation between the γ' particles and the matrix phase, as shown in Fig. 5a. Rather, after images were aligned using cross correlation, two different techniques were employed; either a global threshold method or a custom developed region growing method. The global intensity threshold filter was applied to isolate individual grains as shown in, Fig. 5b. With this method a single intensity threshold was selected and all pixels of the image were interrogated for segmentation. Next a series of dilation and erosion steps were applied to fill in holes in the grain interior due to contrast variations of the γ' particle and feature size threshold was applied to remove spurious data points in other grains, Fig. 5c. Then the boundary was manually inspected and altered to confirm an accurate boundary trace, Fig. 5d. For the grains of similar contrast, a region growing approach was used. In this technique a pixel in the grain interior was selected and the area surrounding that pixel was iteratively expanded to encompass all contacting pixels whose intensities were within a user specified window about the seed pixel's value. With this method, the threshold was only applied to pixels in direct contact with the iteratively growing region. Once an area was selected, a series of dilation and erosion steps using a depth of three pixels were applied to fill in holes in the grain interior caused by contrast variations of the γ' particles, and the accuracy of the boundary was

manually inspected to confirm the boundary trace. A closed surface was constructed from the voxelized boundaries and this surface was smoothed using a smoothing kernel of $3 \times 3 \times 3$ pixels to facilitate visualization.

The individual grains and their boundaries were then visualized using the commercial software Avizo developed by Visualization Sciences Group. In addition to visualizing the data in Avizo, Matlab codes were implemented in the MIPAR software package to analyze macroscopic surface curvature, and the sub micron grain boundary serrations due to the presence of γ' and carbide particles located on the grain boundary surface.

3. Results

Grain boundary sliding volume: The orientations of each grain in the volume were measured with electron backscatter diffraction analysis. The grain boundary misorientation was calculated with respect to the grain 1 coordinate system as $51.7^\circ [1.048 \ 0.009 \ 1.140]$. This high angle grain boundary satisfies the coincidence lattice range requirements for a $\Sigma 11$ special boundary. The criteria for a special boundary are $4\pi[1 - \cos(\theta/\sqrt{n})]$ in axis of misorientation and a range of θ/\sqrt{n} in angular deviation [16], for any of the Σn boundaries with n ranging from 3:31, assuming θ equal to 15° . For $\Sigma 11$, which is characterized as a 50.7° rotation around the $[1 \ 1 \ 0]$ axis, this leads to ranges of 2.24° and 4.52° for the axis and angles of rotation, respectively. The angular difference between the measured boundary axis and angle of misorientation and the axis and angle of misorientation for $\Sigma 11$ are 2.43° and 1° , respectively.

Fig. 6 is a rendering of the surface of the reconstructed grain boundary that experienced GBS. Also shown are deformation twins which appear to emanate from intragranular carbides. Since these structures emanate from the carbides, and are very narrow, the hypothesis is that these are deformation twins and not pre-existing annealing twins. The large twin in the lower right corner of Fig. 6 is not consistent with the other twins in the structure, it is significantly larger than the other deformation twins in all dimensions, and it terminates not only at intragranular carbides but also at a subsurface grain boundary that is not visualized in any of the figures. The dimensions and the termination points of this twin may indicate that this structure is not a deformation twin but instead a pre-existing annealing twin.

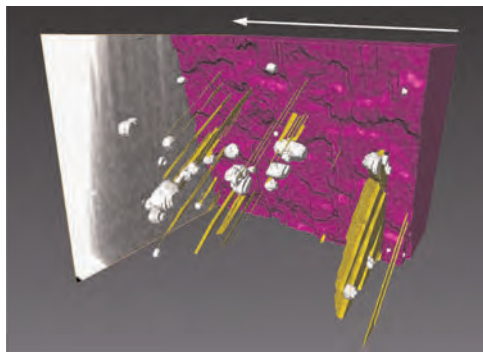


Fig. 6. High angle grain boundary that exhibited GBS, grain 1 is presented as purple and grain 2 is transparent. The deformation twins (yellow) appear to emanate from intragranular carbides (white) and terminate at the grain boundary. The sectioning/sliding direction is presented as a white arrow, and the total dimension of the bounded volume is 6.7 μm along the sectioning direction by 7.8 and 5.6 μm in the image plane. (For interpretation of the references to color in this figure caption, the reader is referred to the web version of this paper.)

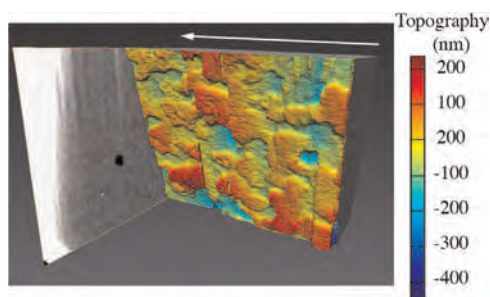


Fig. 7. Topographical color scheme showing variations in surface height based off a fit plane showing connectivity of ridges along the sliding/sectioning direction (presented as a white arrow). The total dimension of the bounded volume is 6.7 μm along the sectioning direction by 7.8 and 5.6 μm in the image plane. (For interpretation of the references to color in this figure caption, the reader is referred to the web version of this paper.)

The grain boundary plane contains both microscale curvature, which is dictated by the grain boundary triple lines, and local serrations due to the γ' structure. To analyze the local serrations of the grain boundary, a plane was fit to the microscale curvature of the grain boundary with an R^2 value of 0.98. A comparison of the fit plane, in the same coordinate system as the EBSD analysis, indicates that the axis of rotation for this $\Sigma 11$ grain boundary creates a 53° angle with the grain boundary normal, indicating that the plane of coincidence is not the grain boundary plane. This indicates that the atomic structure of this grain boundary should not be atomically flat like a coherent $\Sigma 3$ twin boundaries, which is consistent with the observations from Fig. 6. The nanoscale topography was calculated as the difference between each data point and the planar fit. In Fig. 7a, the topological map is overlaid on the original grain boundary surface, and shows the degree to which the local boundary varies from the fit plane surface. Most regions vary between ± 150 nm, with maximum and minimum values of +250 nm and -450 nm, respectively. A comparison of Fig. 7 with Fig. 6 shows that the largest undulations are due to the intergranular carbides and the raised region in the lower right corner of the boundary occurs because the boundary is being pinned by a third grain (not visualized in any of the figures).

This volume did not contain any additional sub surface grain boundaries, assuming of course that the observed twins are caused by deformation and were not present prior to deformation, which is consistent with 2D observations from STEM foils [4]. The nearest triple line was beyond the volume visualized, more than 8.5 μm below the sample surface.

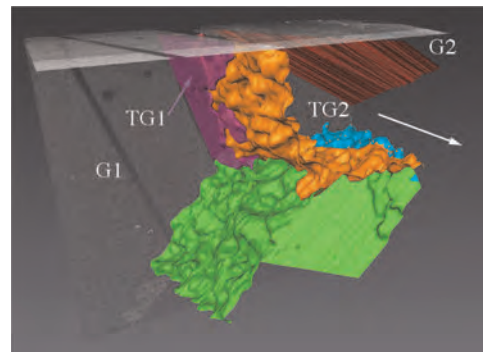


Fig. 8. Serial sectioning data visualized to show the network of grain boundaries in the volume. The sectioning direction is presented as a white arrow, the volume analyzed was 5.5 μm along the sectioning direction and 14.8 by 14.7 μm in the image plane. Each grain boundary is labeled by a user-defined color (purple, red, orange, green, blue). The grain boundary between G1 and TG2 is labeled orange. (For interpretation of the references to color in this figure caption, the reader is referred to the web version of this paper.)

Strain accumulation volume: The volume containing the grain boundary that exhibited strain accumulation was extracted from the location shown in the strain mapped region of Fig. 1b, with the volume location indicated by the rectangular box. The grain boundary network in this region was reconstructed and is shown in Fig. 8. Also presented in Fig. 8 are the grayscale images of the image plane, along the back of the reconstruction, and the composite grayscale image created from the sectioning plane. It can be seen from the top surface that there is excellent alignment of the serial section images as the twin boundary is very linear.

EBSD analysis prior to deformation demonstrates that, except for the $\Sigma 3$ boundaries between grain 1 (G1) and its twin (TG1) and grain 2 (G2) and its twin (TG2), all of the grain boundaries were random high angle grain boundaries (i.e. not Σn with $n > 3$) with misorientation as follows: between G1 G2 is $45^\circ [22\ 7\ 2]$, TG1 G2 is $43.5^\circ [4\ 29\ 0]$, and G1 TG2 is $28^\circ [27\ 2\ 1]$. In all cases the axis of rotation is described in the reference to the orientation of the grain listed first in the sequence. It can be seen in the reconstruction that even though the EBSD map prior to deformation, shown in Fig. 1a, indicated that G1 and G2 are in direct contact on the surface, this is not actually the case since G1 and TG2 are in direct contact in the reconstructed 3D volume. Since the step size in the EBSD characterization was 1 μm , and the thickness of TG2 on the surface was less than 1 μm , the EBSD map could very easily have misidentified the boundary trace on the sample surface between TG2 and G2 in the region of interest.

The microscale curvature of the grain boundary between G1 and TG2 was analyzed by fitting a 2nd order polynomial to the grain boundary surface. Though visually this was a good fit, the R^2 value was only 0.69, indicating that the local serrations lead to substantial differences between the estimated plane and the actual data points. Other polynomial fits (1st through 5th order) were attempted but these did not provide any better R^2 values. Fig. 9 shows the measured local serrations, it can be seen that the peaks and valleys in this grain are on the order of ± 2 μm .

4. Discussion

The automated grain boundary segmentation process used in this study on the ISE images was an *ad hoc* process, and in many cases the steps and settings that worked for segmentation of one grain boundary would not work for another grain boundary. Though the overall steps worked on multiple grain boundaries, the user defined thresholds and windows needed to be changed for each feature segmented due to variations in contrast between

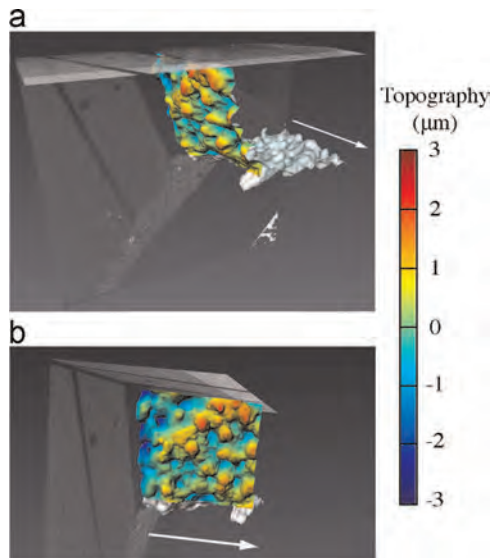


Fig. 9. Local serration measurements overlaid on the original grain boundary surface between TG2 and G1. (a) at the same specimen orientation presented in Fig. 8, and (b) with the volume rotated for a better view of the surface topography. The sectioning direction is presented as a white arrow, the volume analyzed was 5.5 μm along the sectioning direction and 14.8 by 14.7 μm in the image plane. (For interpretation of the references to color in this figure caption, the reader is referred to the web version of this paper.)

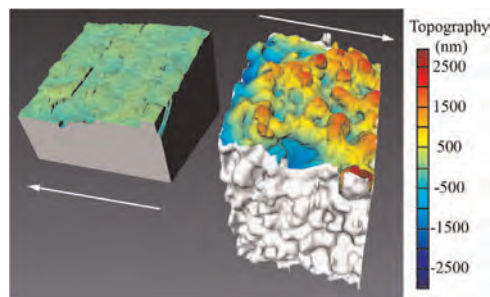


Fig. 10. Grain boundary topography for the boundary that experienced GBS (left) and the boundary that experienced strain accumulation (right) presented using the same color scale. The arrows indicate the sectioning directions. (For interpretation of the references to color in this figure caption, the reader is referred to the web version of this paper.)

features of interest. The most difficult grains to segment were those for which the γ' particles had slightly different intensities than the grain matrix. Even though automated segmentation was conducted, every slice was manually inspected to insure proper grain boundary structure was identified.

It has been shown that the deliberate creation of grain boundary serrations on the order of tens of μm limits the activity of the GBS mechanism in these materials [6]. It has also been hypothesized that the mechanism of GBS active in this temperature range should be Rachinger sliding, which is accompanied by the intragranular movement of dislocations [17]. Therefore, it is expected that preexisting nm scale serrations might also affect the propensity of GBS. Additional work is necessary to statistically quantify the grain boundary serrations, both pre and post deformation to conclusively determine if this structure is important to facilitating GBS. If it is assumed that the serrations in both grain boundaries were present prior to deformation, it can be seen that there are substantial differences in grain boundary topography. When presented using the same topography legend, Fig. 10, one can see that the serrations in the grain boundary that experienced strain accumulation are an order of magnitude greater than the

boundary that experienced GBS. These results are consistent with measurements of local serrations measured from STEM foils that experienced strain accumulation and GBS [4].

The other striking difference between the two different grain boundary structures was the relative simplicity of the sub surface grain boundary network that experienced GBS versus the complexity of the grain boundary neighborhood of the grain boundary that experienced strain accumulation. The grain boundary that experienced strain accumulation had several other sub surface grain boundaries in close proximity ($<6 \mu\text{m}$), while the boundary that experienced GBS was a single continuous boundary free of sub surface grain boundaries ($>8.5 \mu\text{m}$), as measured by a line in a slice plane, perpendicular to the sample surface. These results are consistent with observations from STEM foils and areas FIB cross sectioned for boundary observations, and with observations from the full field strain maps that indicate that strain localization sites readily occur at grain boundary triple points [6,7].

5. Conclusions

The use of a dual beam FIB for 3 D serial sectioning proved to be a valuable tool for exploring grain boundary sub surface structure. A technique was developed to characterize the local serrations of the grain boundaries by first removing the macroscale boundary curvature. The analysis indicated that a grain boundary which exhibited GBS was planar on the macroscale and had local serrations on the order of the secondary γ' particle size. The grain boundary that experienced strain accumulation was a component of a very complex local network of sub surface grain boundaries. The local serrations on this grain boundary were an order of magnitude greater than that measured on the boundary that experienced GBS.

Strain accumulation occurs readily at $\Sigma 3$ annealing twins and random high angle grain boundaries early in the deformation of René 104 [6]. The serial sectioning reconstructions indicate that localization of strain at these random high angle grain boundaries might be associated with the proximity of the sub surface grain boundaries, particularly the presence of $\Sigma 3$ annealing twins. The reconstructed data also seems to confirm that the local serrations at grain boundaries play a role in the likelihood of grain boundaries to experience GBS. More observations of both types of grain boundaries are needed to provide further support of these hypotheses.

Acknowledgments

Funding was provided by the Air Force Research Laboratory (AFRL) STW 21 Program FA9550 09 1 0014.

References

- [1] R.C. Reed, *The Superalloys: Fundamentals and Applications*, University Press, New York, 2006.
- [2] S. Ghosh, M.K. Samal, Multiscale Crystal Plasticity Modeling of Microtwinning Induced Deformation in Gamma–Gamma Prime Nickel Based Superalloys, Shanghai University, Shanghai, Peoples Republic of China, 2011, pp. 487–488.
- [3] H. Deuchman, P.J. Phillips, N. Zhou, M. Samal, S. Ghosh, Y. Wang, M.J. Mills, Deformation mechanisms coupled with phase field and crystal plasticity modeling in a high temperature polycrystalline nickel-based superalloy, in: *Superalloys 2012*, 2012, p. 25.
- [4] J. Carter, N. Zhou, J. Sosa, P. Shade, A. Pilchak, M. Kuper, Y. Wang, H. Fraser, M. Uchic, M. Mills, Characterization of strain accumulation at grain boundaries of nickel-based superalloys, in: *Superalloys 2012*, TMS, Warrendale, PA.
- [5] T. Turner, P. Shade, M. Groeber, M. Miller, M. Uchic, Two integrated experimental and modeling approaches to study strain distributions in nickel and nickel-base superalloy polycrystals, in: *Models for Processing and Properties*, The Minerals, Metals and Materials Society, Seven Springs, PA, 2012, p. 643–652.

- [6] J. Carter, M. Kuper, M. Uchic, M. Mills, Characterization of localized deformation near grain boundaries of superalloy rené-104 at elevated temperature, *Mater. Sci. Eng.: A* 605 (2014).
- [7] J. Carter, Exploration of local strain accumulation in nickel-based superalloys (Vol. Ph.D. dissertation), The Ohio State University, Materials Science and Engineering, URL https://etd.ohiolink.edu/ap:10:0::NO:10:P10_ACCESSION_NUM:osu1344646905, 2013.
- [8] J.L. Walley, R. Wheeler, M.D. Uchic, M.J. Mills, In situ mechanical testing for characterizing strain localization during deformation at elevated temperatures, *Exp. Mech.* 52 (4) (2011) 405–416, <http://dx.doi.org/10.1007/s11340-011-9499-7>, URL <http://link.springer.com/10.1007/s11340-011-9499-7>.
- [9] M.H.F. Overwijk, F.C. Vandenheuvel, C.W.T. Bullelieuwma, Novel scheme for the preparation of transmission electron-microscopy specimens with a focused ion-beam, *J. Vac. Sci. Technol. B* 11 (6) (1993) 2021–2024, <http://dx.doi.org/10.1116/1.586537>, URL WOS:A1993MM97200011.
- [10] M.D. Uchic, M.A. Groeber, D.M. Dimiduk, J. Simmons, 3D microstructural characterization of nickel superalloys via serial-sectioning using a dual beam FIB-SEM, *Scr. Mater.* 55 (1) (2006) 23–28, <http://dx.doi.org/10.1016/j.scripta-mat.2006.02.039>, URL <http://linkinghub.elsevier.com/retrieve/pii/S1359646206001564>.
- [11] J. Sosa, D. Huber, B. Welk, H. Fraser, Development and application of MIPAR, *Integr. Mater. Manuf. Innov.* 3 (2014) 1–18.
- [12] L. Vincent, P. Soille, Watersheds in digital spaces—an efficient algorithm based on immersion simulations, *Ieee Trans. Pattern Anal. Mach. Intell.* 13 (6) (1991) 583–598, <http://dx.doi.org/10.1109/34.87344>, URL WOS:A1991FU37200007.
- [13] J.B. Roerdink, A. Meijster, The watershed transform: definitions, algorithms and parallelization strategies, *Fundam. Inf.* 41 (1) (2000) 187–228, URL <http://iospress.metapress.com/index/X72176151257WH4M.pdf>.
- [14] L. Najman, M. Couprie, G. Bertrand, Watersheds, mosaics, and the emergence paradigm, *Discr. Appl. Math.* 147 (2–3) (2005) 301–324, <http://dx.doi.org/10.1016/j.dam.2004.09.017>, WOS:000228118600010.
- [15] D.J. Rowenhorst, A.C. Lewis, G. Spanos, Three-dimensional analysis of grain topology and interface curvature in a α & β -titanium alloy, *Acta Mater.* 58 (16) (2010) 5511–5519, URL http://journals.ohiolink.edu/ejc/article.cgi?issn=13596454&issue=v58i0016&article=5511_taogtaiciaa.
- [16] D.G. Brandon, The structure of high-angle grain boundaries, *Acta Metal.* 14 (11) (1966) 1479–1484, URL <http://www.sciencedirect.com/science/article/pii/0001616066901684>.
- [17] T.G. Langdon, Grain boundary sliding revisited: developments in sliding over four decades, *J. Mater. Sci.* 41 (3) (2006) 597–609, <http://dx.doi.org/10.1007/s10853-006-6476-0>, URL <http://link.springer.com/10.1007/s10853-006-6476-0>.